



Effect of cation and anion doping on microstructure and electrochemical properties of the $\text{LiMn}_{1.5}\text{Ni}_{0.5}\text{O}_{4-\delta}$ spinel

Nader M. Hagh*, Glenn G. Amatucci

Energy Storage Research Group (ESRG), Department of Materials Science and Engineering, Rutgers, The State University of New Jersey, 671 US Highway 1, North Brunswick, NJ 08902, USA

HIGHLIGHTS

- Fluorine doped spinel with disordered structure showed much improved capacity retention with cycle number over pristine 4.7 V spinel at 60 °C.
- Li and F doping were optimized relative to the formation of ordered ($\text{P}4_3\text{3}2$) and disordered spinel ($\text{Fd}-\text{3}m$), respectively.
- Two distinctive effects of Li and fluorine doping were demonstrated on particle size and surface area of the spinel.

ARTICLE INFO

Article history:

Received 15 November 2013

Received in revised form

17 December 2013

Accepted 31 December 2013

Available online 23 January 2014

ABSTRACT

A detailed investigation of the structural and electrochemical impact of lithium and fluorine substitutions on the 4.7 V $\text{LiMn}_{1.5}\text{Ni}_{0.5}\text{O}_{4-\delta}$ (LMNO) positive electrode for Li-ion batteries was accomplished. Impact of subsequent transition metal substitution on the tetrahedral 8a sites was also investigated relative to rate and elevated temperature cycling stability. Significantly improved cycling in excess of 600 cycles was established for an anion modified spinel relative to an optimized benchmark material at 60 °C.

© 2014 Elsevier B.V. All rights reserved.

Keywords:

Li-ion

Spinel

High voltage cathode

Secondary battery

Cation and anion doping

Elevated temperature cycling

1. Introduction

The growing demand for electrochemical energy storage systems with higher volumetric and gravimetric energy densities have highlighted secondary lithium ion batteries as a viable candidate for numerous applications in consumer electronics, biomedical, telecommunication, military, automotive industry, and even grid application. Increase of energy density can be reached by higher capacity and/or higher voltage cells. The latter requires the development of new, high voltage positive electrode materials. One of the most promising high voltage positive electrodes, is cation doped $\text{LiM}_x\text{Mn}_{2-x}\text{O}_4$ spinel where $M = \text{Ni}$ [1–5], Cr [6], Fe [7], Cu [8], Co [9,10], or co-doping with Ni–Mo [11], Ni–Mg [12], and Ni–Fe

[13] in octahedral site of Mn. The electrochemical performance of $\text{LiM}_x\text{Mn}_{2-x}\text{O}_4$ spinel is directly affected by the type and amount of doped atom either in ordered 4b and 12d octahedral sites ($\text{P}4_3\text{3}2$ space group) or in randomly occupied 16d sites ($\text{Fd}-\text{3}m$) of the cubic structure. Among different dopants, Ni doped spinel ($\text{LiNi}^{2+}_{0.5}\text{Mn}^{4+}_{1.5}\text{O}_4$; LMNO) is of special interest since it shifts the voltage profile of the parent composition (LiMn_2O_4) to a higher potentials by introducing new voltage plateaus at 4.4–4.7 V and 4.7–5.0 V (corresponding to $\text{Ni}^{2+}/\text{Ni}^{3+}$ and $\text{Ni}^{3+}/\text{Ni}^{4+}$ redox reactions, respectively). In terms of electrochemical performance, this substitution for Mn provides relatively good room temperature reversible cycling ($\geq 95\%$ of theoretical capacity) with good rate capability in conventional electrolyte (e.g. $\text{LiPF}_6/\text{EC-DMC}$). However despite the promising room temperature performance, the LMNO spinel experiences a large capacity loss followed by early cell failure at elevated temperature which is critical for HEV/PHEV applications. Although there have been several reports on elevated temperature performance of $\text{LiMn}_{1.5}\text{Ni}_{0.5}\text{O}_4$ [14,15], the prolonged

* Corresponding author. Present address: NEI Corporation, 400 E Apgar Dr., Somerset, NJ 08873, USA.

E-mail address: nmhagh@gmail.com (N.M. Hagh).



cycling of LMNO at elevated temperature is still suffering from a significant impedance rise.

It is believed that the poor electrochemical performance at elevated temperature is associated with electrolyte–electrode interface side reactions which control the stability of the cell. There have been numerous reports on minimizing the electrolyte–electrode interface reactivity by coating the surface of the cathode through thin layer of ZnO [16], SiO₂ [17], Al₂O₃, MgO, LiCoO₂ [18], and Au [19], or surface treatment of the cathode by mild acidic solutions [20,21]. In all these efforts, the improved electrode–electrolyte interface stability was achieved through modification in the surface chemistry of the electrode. An alternative way to achieve interface stability is through intrinsic stabilization of the spinel towards reactions with the electrolyte, even if preferentially located at the surface. Substitution of oxygen by fluorine in the spinel structure has been first reported for parent composition of Li_{1+x}Mn₂O₄ along with co-doping of Al and F in Mn and O sites respectively, which improved capacity retention and cycling stability at elevated temperature [22–25]. Improvements in electrochemical and thermal stability of spinel materials [26–28] and

layered-structured oxides [29–31] were also reported upon fluorine substitution in oxygen sites.

In the current paper, we systematically study the effect of excess Li as well as oxygen substitution by fluorine on physical, microstructure and electrochemical properties of Li_{1+y}Mn_{1.5}Ni_{0.5}O_{4-x}F_x ($0 \leq x \leq 0.5$, $0 \leq y \leq 0.3$) spinel processed through our newly developed two-step solid state synthesis technique [32]. In this process, the synthesis of spinel powder was carried out by pre-reacting of NiO with MnO₂ at high temperatures (900 °C–3 h) followed by incorporating of the Li into the nickel manganese oxide (Ni_{1-x}Mn₂O₄) structure at subsequent heat treatment (800 °C–12 h).

2. Experimental

Li_{1+y}Mn_{1.5}Ni_{0.5}O_{4-x}F_x ($0 \leq x \leq 0.5$, $0 \leq y \leq 0.3$) spinels were prepared by conventional solid-state process. First, the stoichiometric amounts of NiO and MnO₂ were thoroughly mixed using the zirconia milling media and anhydrous Acetone as a medium for 24 h followed by drying at 110 °C for 12 h. The dried powder was

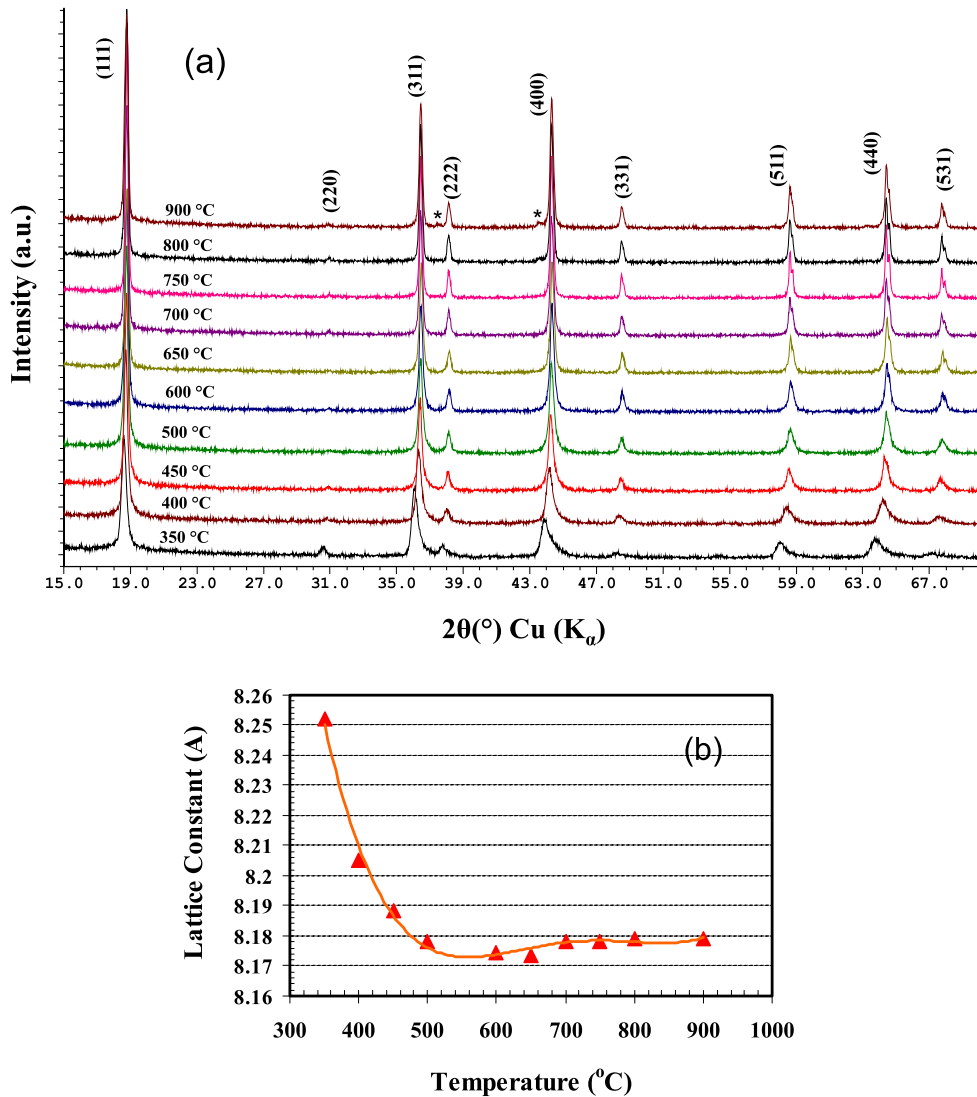


Fig. 1. (a) X-ray diffraction patterns and (b) lattice parameter changes during the formation of the LiMn_{1.5}Ni_{0.5}O_{4-δ} spinel at annealing temperatures of 350 °C–900 °C; (*: second phase Li_xNi_{1-x}O₂ or Ni₆MnO₈).

Table 1

Effect of F^- and excess Li^+ addition on surface area of the $LiMn_{1.5}Ni_{0.5}O_{4-\delta}$ spinel.

| F^- substitution (x in $LiMn_{1.5}Ni_{0.5}O_{4-x}F_x$) | $x = 0$ | $x = 0.1$ | $x = 0.2$ | $x = 0.3$ | $x = 0.4$ | $x = 0.5$ |
|--|-----------------|-----------------|-----------------|-----------------|-----------------|-----------------|
| BET surface area ($m^2 g^{-1}$) | 2.50 ± 0.01 | 2.12 ± 0.01 | 1.82 ± 0.01 | 1.71 ± 0.01 | 1.96 ± 0.01 | 2.05 ± 0.01 |
| Excess Li^+ (y in $Li_{1+y}Mn_{1.5}Ni_{0.3.8}F_{0.2}$) | $y = 0$ | $y = 0.1$ | $y = 0.15$ | $y = 0.2$ | $y = 0.3$ | |
| BET surface area ($m^2 g^{-1}$) | 1.66 ± 0.01 | 1.68 ± 0.01 | 1.91 ± 0.01 | 1.91 ± 0.01 | 2.01 ± 0.01 | |

heat treated at 900 °C for 3 h in order to form $Ni_{1-x}Mn_2O_4$ ($x \leq 0.33$) spinel. The appropriate moles of Li_2CO_3 and LiF were mixed with $Ni_{1-x}Mn_2O_4$ ($x \leq 0.33$) powder through the similar wet ball milling procedure. After drying the mixture at 110 °C for 12 h, the powder was heat treated in 800 °C for 12 h [32].

A Scintag X-ray diffractometer with $Cu K\alpha$ X-ray source was utilized to characterize the phase type of the synthesized powders. For lattice parameter, internal silicon standard was used. The multipoint Brunauer–Emmett–Teller (BET) surface area was measured by Micromeritics ASAP 2010 surface area analyzer. SEM and EDS studies of powders were carried out by field emission scanning electron microscopy (FESEM; LEO (ZEISS) 982) using the accelerating voltage of 5.0 kV.

Structural analysis of the spinel powders was carried out using Rietveld analysis to determine the occupancy and metal ion distribution in tetrahedral and octahedral sites of the pristine and doped spinels. The refinement was performed by considering the space group of Fd-3m for all pristine and doped materials, since the profile fit showed a better match with disordered Fd-3m space group than ordered P4₃32 spinel. In addition, the occupancy for oxygen atom was selected one (full occupancy) and atomic displacement was considered $B_{iso} = 0.5$. Refinement was carried out by considering partial occupancy for Ni in 8a tetrahedral sites.

For electrochemical characterization, 2032 coin type stainless steel and Al plated stainless steel cells were utilized. Each cell was consisted of cathode spinel material, anode (Li metal) and electrolyte, 1 M $LiPF_6$ dissolved in mixture of ethylene carbonate – dimethyl carbonate (EC-DMC). The positive electrode tape was prepared through the tape casting of 52 wt% active spinel cathode material, 13 wt% Super P, and 35 wt% PVDF-HFP (Polyvinylidene fluoride hexafluoro propylene) binder with DBP (Dibutyl Phthalate) as a plasticizer. The plasticizer was extracted from the electrode prior to use by successive extractions in anhydrous di-methyl ether. The relatively low active content was utilized to be sure that the electrode formulation was not the limiting factor in the electrochemistry of the materials. We do not intend to show data that have failure induced by the breakdown of the percolation network/

binder in the electrode vs the phenomena associated with the material itself. The prepared cathode tape was assembled in He-filled glove box and cycled using a MacCor galvanostat cycler. The charge–discharge cycling of the cells was achieved between 3.5 V and 5.0 V at the cycling rates of 44–2864 mA g⁻¹.

3. Results and discussions

3.1. Solid-state synthesis of spinel

The X-ray diffraction patterns of $LiMn_{1.5}Ni_{0.5}O_4$ spinel heat treated at temperature ranges of 350 °C–900 °C is illustrated in Fig. 1a. As shown, the formation of $LiMn_{1.5}Ni_{0.5}O_4$ spinel was initiated from 400 °C with the presence of slightly asymmetrical peaks which could represent the existing of disordered structure with the possibility of having second phase(s). Despite this, there was no distinguishable second phase even at fabrication temperatures as low as 350 °C. The calculated crystallite size based on Scherrer equation was ~23 nm at temperature of 350 °C. The presence of large (220) peak at 350 °C indicates the existence of transition metal ions (likely Ni^{2+} based on ligand theory) in the 8a tetrahedral sites due to their larger scattering factor relative to Li ion. Increasing the annealing temperature systematically increased the (111)/(220) ratio up to 500 °C which implies that Ni or Mn ions or both were possibly migrated from tetrahedral sites of (220) to (111) plane where the metal ions generally reside in the ordered and disordered form of spinel. At temperature range of 500 °C < $T \leq 900$ °C, (111)/(220) ratio approaches to a plateau with less variation in the relative intensity value indicating the relative stability in metal ion rearrangement. The appearance of the second phases in the form of $Li_xNi_{1-x}O_2$ and Ni_6MnO_8 was detected at higher annealing temperatures namely $T \geq 800$ °C, where the severe oxygen and lithium loss disintegrates the stoichiometric spinel structure as has been noted previously [33]. The transition metal occupancy on the 8a site was investigated with greater detail using Rietveld analysis. Results of Table 3 are consistent with the qualitative results described above.

Table 2

Structural and electrochemical performance of $Li_{1+y}Mn_{1.5}Ni_{0.5}O_{4-x}F_x$ ($0 \leq x \leq 0.5$, $0 \leq y \leq 0.3$) spinels at 24 °C and 60 °C.

| Composition | Lattice parameter (Å) | ^a IDC (mAh/g) | ^b Capacity loss(–)/Gain(+) (%) | | | | ^c Columbic efficiency (%) | |
|---|-----------------------|--------------------------|---|--------|-------------------|--------|--------------------------------------|-------|
| | | | 50 th | | 100 th | | 24 °C | 60 °C |
| | | | 24 °C | 60 °C | 24 °C | 60 °C | | |
| $LiMn_{1.5}Ni_{0.5}O_4$ | 8.1845 | 114.7 | (–)2.8 | (–)3.2 | (–)4.3 | (–)6.5 | 99.4 | 96.9 |
| $LiMn_{1.5}Ni_{0.5}O_{3.9}F_{0.1}$ | 8.1934 | 111.8 | (+)1.3 | (+)1.4 | (+)0.5 | – | 99.1 | 97.1 |
| $LiMn_{1.5}Ni_{0.5}O_{3.8}F_{0.2}$ | 8.2037 | 107.0 | (+)4.6 | (+)2.8 | (+)4.3 | (+)2.2 | 99.2 | 98.0 |
| $LiMn_{1.5}Ni_{0.5}O_{3.7}F_{0.3}$ | 8.2183 | 92.2 | (+)8.6 | (+)5.2 | (+)8.7 | – | 99.1 | 97.0 |
| $LiMn_{1.5}Ni_{0.5}O_{3.6}F_{0.4}$ | 8.2119 | 90.7 | (+)8.1 | (+)3.5 | – | – | 99.2 | 96.9 |
| $LiMn_{1.5}Ni_{0.5}O_{3.5}F_{0.5}$ | 8.2215 | 92.6 | (+)12.5 | (+)7.6 | – | – | 99.0 | 96.0 |
| $LiMn_{1.5}Ni_{0.5}O_{3.8}F_{0.2}$ | 8.2037 | 107.0 | (+)4.6 | (+)2.7 | (+)4.3 | (+)2.3 | 99.2 | 97.1 |
| $Li_{1.1}Mn_{1.5}Ni_{0.5}O_{3.8}F_{0.2}$ | 8.1870 | 112.1 | (+)1.8 | (+)0.3 | (+)1.2 | (–)1.0 | 99.2 | 97.4 |
| $Li_{1.15}Mn_{1.5}Ni_{0.5}O_{3.8}F_{0.2}$ | 8.1802 | 130.8 | (–)0.9 | (–)3.0 | (–)2.1 | – | 99.4 | 97.0 |
| $Li_{1.2}Mn_{1.5}Ni_{0.5}O_{3.8}F_{0.2}$ | 8.1740 | 129.3 | (–)2.4 | (–)3.7 | – | – | 99.3 | 97.2 |
| $Li_{1.3}Mn_{1.5}Ni_{0.5}O_{3.8}F_{0.2}$ | 8.1695 | 126.0 | (–)3.7 | (–)5.0 | (–)6.9 | – | 99.2 | 96.7 |

^a Initial discharge capacity at room temperature (24 °C).

^b Discharge capacity loss/gain relative to first cycle.

^c Columbic efficiency at cycle 10.

Table 3

Summary of structural refinement and physical properties of the refined pristine and doped spinels (F: Fluorine, L: Li).

| Atom | Wyckoff | Occupancy (n) | | | | | | | | | |
|------------------------------|---------|---------------|---------|---------|---------|---------|---------|-------------|--------------|-------------|-------------|
| | | 0 F | 0.1 F | 0.2 F | 0.3 F | 0.4 F | 0.5 F | 0.1 L–0.2 F | 0.15 L–0.2 F | 0.2 L–0.2 F | 0.3 L–0.2 F |
| Li1 | 8a | 0.96115 | 0.93023 | 0.88016 | 0.84023 | 0.87034 | 0.84037 | 0.9403 | 0.96057 | 0.96996 | 0.98899 |
| Ni1 | 8a | 0.0401 | 0.07002 | 0.12002 | 0.16002 | 0.13003 | 0.16003 | 0.06003 | 0.04006 | 0.03 | 0.00992 |
| Mn | 16d | 0.75026 | 0.75 | 0.75 | 0.75 | 0.75 | 0.75 | 0.75 | 0.75017 | 0.75 | 0.75021 |
| Ni2 | 16d | 0.2302 | 0.21503 | 0.19 | 0.17004 | 0.18504 | 0.17004 | 0.22003 | 0.23013 | 0.23502 | 0.24516 |
| O | 32e | 1 | 1 | 1 | 1 | 1 | 1 | 1 | 1 | 1 | 1 |
| Li2 | 16d | 0.02239 | 0.035 | 0.06041 | 0.08046 | 0.06544 | 0.08045 | 0.03032 | 0.0215 | 0.01522 | 0.00691 |
| R_{wp} (%) | | 4.93 | 4.22 | 5.07 | 5.65 | 4.99 | 5.16 | 4.57 | 4.52 | 3.92 | 4.1 |
| E_{exp} (%) | | 0.87 | 0.67 | 0.70 | 0.72 | 0.68 | 0.72 | 0.69 | 0.70 | 0.67 | 0.69 |
| GOF (R_{wp}/E_{exp}) | | 5.67 | 6.29 | 7.24 | 7.84 | 7.33 | 7.17 | 6.62 | 6.46 | 5.85 | 5.94 |
| a (Å) | | 8.17529 | 8.18963 | 8.2003 | 8.21756 | 8.20548 | 8.21623 | 8.18501 | 8.1733 | 8.16964 | 8.16576 |
| Vol. (Å ³) | | 546.4 | 549.3 | 551.4 | 554.9 | 552.5 | 554.6 | 548.4 | 546.0 | 545.3 | 544.5 |
| ρ (g cm ⁻³) | | 4.4439 | 4.4184 | 4.4014 | 4.3738 | 4.3933 | 4.3759 | 4.4257 | 4.4462 | 4.4509 | 4.4584 |

The effect of annealing temperature on lattice parameter of the two-step solid state process is illustrated in Fig. 1b. The sharp decrease in lattice parameter up to 650 °C followed by slight increase up to 900 °C implied the existence of larger Mn³⁺ rich ion at lower temperatures. As reported by Zhong et al. [3], when the annealing temperature approached to 600 °C, the average Mn

oxidation state in LiMn_{1.5}Ni_{0.5}O₄ spinel prepared by sol–gel was increased to 3.97, along with a decrease in lattice parameter. This behavior paralleled what we have observed as our annealing temperatures approached to $T = 650$ °C.

At higher temperatures ($T \geq 650$ °C), reduction in Mn valence (Mn⁴⁺ to Mn³⁺) is responsible for the slight expansion in the lattice

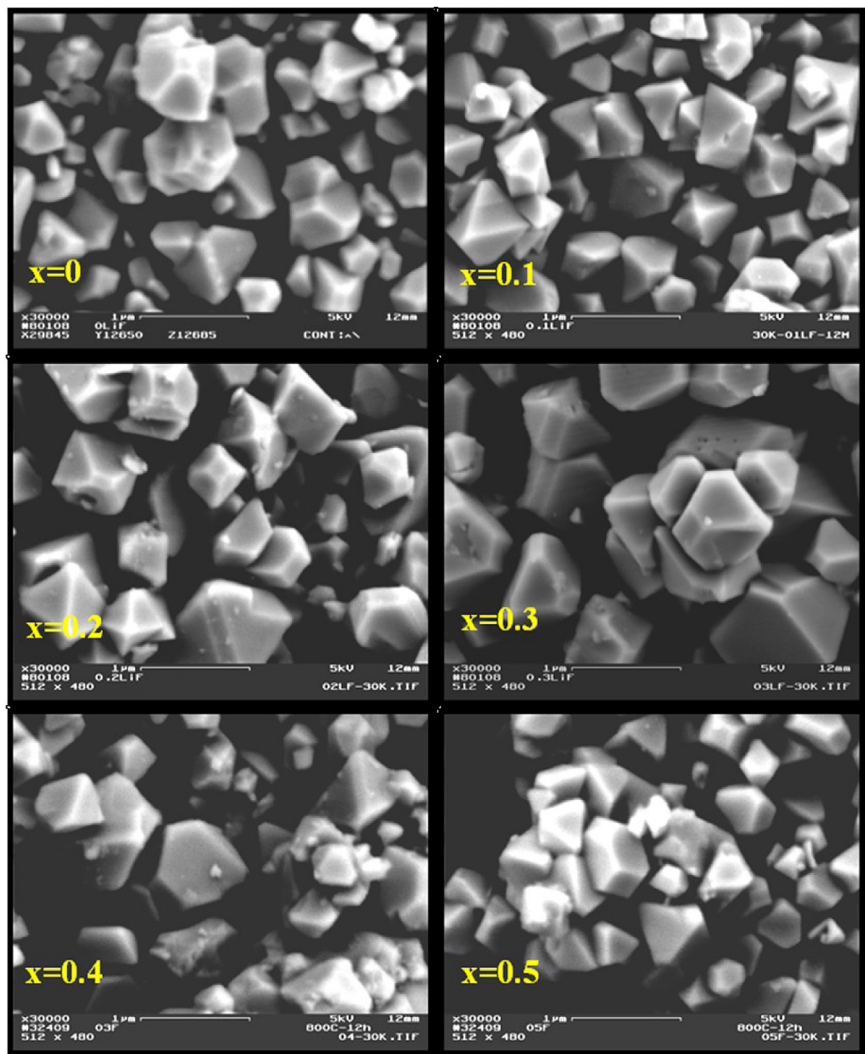


Fig. 2. Field emission scanning electron microscopy (FESEM) micrographs of LiMn_{1.5}Ni_{0.5}O₄–xF_x ($x = 0, 0.1, 0.2, 0.3, 0.4$, and 0.5) spinels annealed at 800 °C–12 h.

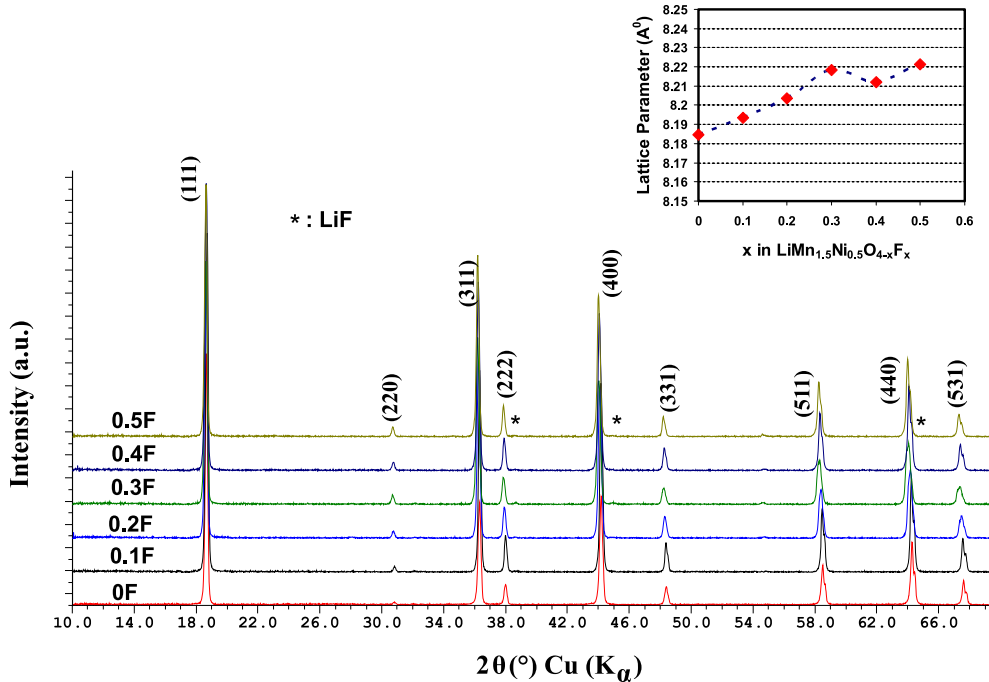


Fig. 3. X-ray diffraction of the fluorine (x) doped $\text{LiMn}_{1.5}\text{Ni}_{0.5}\text{O}_{4-x}\text{F}_x$ spinel ($x = 0, 0.1, 0.2, 0.3, 0.4, 0.5$) annealed at $800 \text{ }^{\circ}\text{C}$ -12 h.

structure. This reduction is induced by the oxygen loss followed by the subsequent formation of the second phases from the pure spinel $\text{LiMn}_{1.5}\text{Ni}_{0.5}\text{O}_4$ in the form of $\text{Li}_x\text{Ni}_{1-x}\text{O}_2$ or nickel manganese oxide. In addition, higher annealing temperatures formed well-faceted crystalline particles at the expense of particle growth (lowering the surface area) and possibly sacrificing the capacity. Although this low surface area improves the long term stability of the cathode by reducing the cathode–electrolyte interface, cell failure still persists through the dissolution of cathode into the electrolyte and forming the large impedance [21]. One approach to improve the cathode's stability of low surface area spinel is intrinsic modification through either cation (Li) or anion (F) substitution. In the following section the effect of F and co-doping with Li and F on microstructure and electrochemical performance of spinel is systematically studied.

3.2. Oxygen substitution by fluorine in $\text{LiMn}_{1.5}\text{Ni}_{0.5}\text{O}_{4-x}\text{F}_x$

Fig. 2 illustrates the SEM micrograph of 0–0.5 nominal mol.% fluorine-doped $\text{LiMn}_{1.5}\text{Ni}_{0.5}\text{O}_4$ annealed at $800 \text{ }^{\circ}\text{C}$ for 12 h to show the effect of fluoride on the particle size and morphology of the spinel. Introduction of fluorine led to a formation of large well-faceted crystalline particles. This is mainly due to a fluxing effect of LiF with the melting point of $\sim 848 \text{ }^{\circ}\text{C}$ (in a proximity of our heat treatment temperature; $800 \text{ }^{\circ}\text{C}$ -12 h) which led to a growth of large faceted particles during cooling. The final particle morphology was corresponding to a typical octahedral shape of (111) faceted planes. Fluorine substitution resulted in the decrease of the surface area (Table 1) consistent with the observed increase in crystallinity and smoothness of the facets. In the case of 0.3 mol of fluorine, surface area decreased from $2.50 \text{ m}^2 \text{ g}^{-1}$ to about $1.7 \text{ m}^2 \text{ g}^{-1}$.

The crystal structure of the LMNO was also affected by fluorine substitution. As shown in Fig. 3 all x-ray patterns demonstrated the spinel as a major phase with space group of $\text{Fd}-3\text{m}$. Introduction of fluorine shifted the x-ray patterns toward lower angles or higher d-spacing which indicated an expansion of the lattice structure as

shown in Table 2. Monovalent fluorine substitution in divalent oxygen could change the charge balance in spinel by reducing the Mn^{4+} to Mn^{3+} . The increase in concentration of Mn^{3+} ions with larger ionic radius (0.58 \AA for low and 0.65 \AA for high spin manganese) relative to smaller Mn^{4+} (0.53 \AA) led to an expansion of lattice structure. However, it is important to note that the fluorine substitution also increased the number of tetrahedral sites occupied by metal ions, namely Mn and Ni ions. This could be shown either through (311)/(111) intensity ratio of the spinel as reported by Tarascon et al. in LiMn_2O_4 [34] or through (220) diffraction intensity which reflects the type of ions residing in the tetrahedral sites of the spinel. As shown in Fig. 4, introducing the fluorine raised the (311)/(111) intensity ratio as well as relative intensity of (220). This indicates that fluorine substitution enabled more metal ions to be removed from octahedral sites and occupy tetrahedral sites of the spinel. As such, this lends to the theory that not all Li from the LiF is being substituted into the spinel. This would leave a non stoichiometric spinel that would result in a structure with vacancies present on the 8a tetrahedral sites. As this configuration

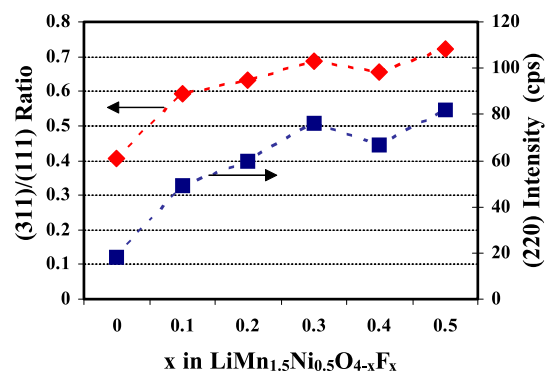


Fig. 4. X-ray (311)/(111) and (220) peak intensity ratios for the fluorine doped $\text{LiMn}_{1.5}\text{Ni}_{0.5}\text{O}_{4-x}\text{F}_x$ spinels ($x = 0, 0.1, 0.2, 0.3, 0.4$, and 0.5) annealed at $800 \text{ }^{\circ}\text{C}$ -12 h.

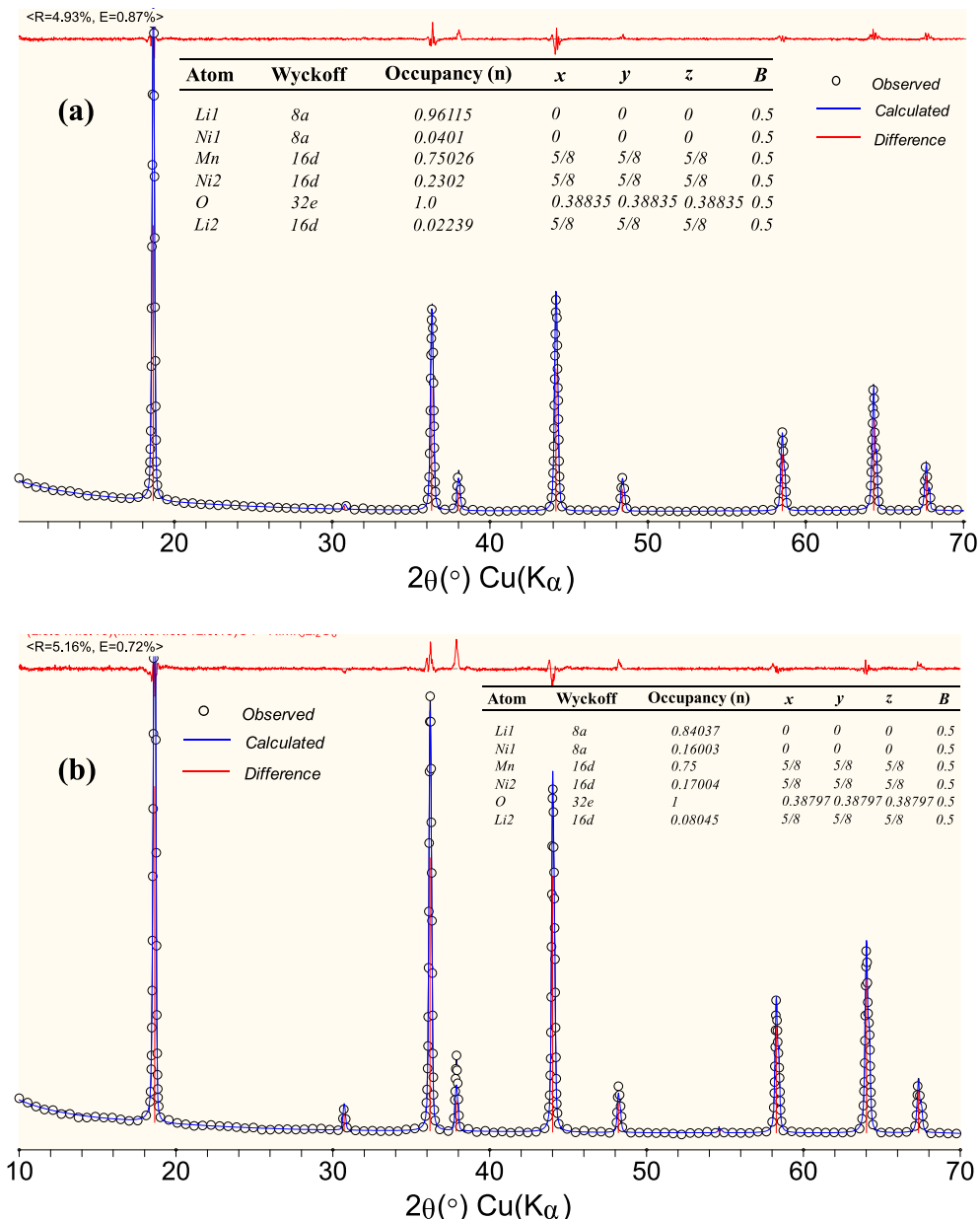


Fig. 5. Structural refinement of (a) pristine spinel $\text{Li}[\text{Mn}_{1.5}\text{Ni}_{0.5}]\text{O}_{4-\delta}$ (R_{wp} : 4.93%, E : 0.87%, S.G.: Fd-3m, no. 227 or cF56.1; origin at $-43m$; $a = 8.17529 \text{ \AA} \pm 0.000136$; Cell vol. = 546.4 \AA^3 ; $\rho = 4.4439 \text{ g cm}^{-3}$) and (b) 0.5 Fluorine doped spinel ($\text{LiMn}_{1.5}\text{Ni}_{0.5}\text{O}_{3.5}\text{F}_{0.5}$) by Rietveld analysis (R_{wp} : 5.16%, E : 0.72%; S.G.: Fd-3m, no. 227 or cF56.1; origin at $-43m$; $a = 8.21623 \text{ \AA} \pm 0.000157$; Cell vol. = 554.6 \AA^3 ; $\rho = 4.3759 \text{ g cm}^{-3}$).

would be assumed to be energetically unstable, Ni^{2+} from the 16d sites are likely to occupy the tetrahedral sites along with Li leading to a general formula of $(\text{Li}_{1-v}\text{Ni}_v)_{8a}[\text{Ni}_{0.5-v}\text{Mn}_{1.5}]_{16d}(\text{O}_4)_{32e}$; ($v > 0$). If this occurs the overall charge balance would lead toward the increase in quantity of Mn^{3+} . The formation of this larger ion would subsequently and systematically increase the lattice parameter as is observed in Fig. 3.

The structural refinement of pristine and fluorine-doped spinels (0F, 0.1F, 0.2F, 0.3F, 0.4F, and 0.5F) was carried out by partial Ni and Li occupancy in 8a and 16d sites, respectively, utilizing the disordered structure (Fd-3m), full oxygen occupancy and a constant isotropic atomic displacement ($B_{iso} = 0.5$). Table 3 shows a summary of structural refinement for pristine and all fluorine-doped spinels (0F, 0.1F, 0.2F, 0.3F, 0.4F, and 0.5F). As shown, the whole pattern fitting (R_{wp}) was in the range of 4.22–5.65% which showed

a good agreement between observed and refined patterns. In addition, the refinement results for all powders, including undoped spinel, showed certain degrees of metal ion mixing including Ni atom migration to 8a tetrahedral sites and Li atoms into the 16d sites of octahedral coordination. Table 3 also shows that the fluorine substitution further increased the concentration of Ni atoms at tetrahedral sites of the cubic spinel. This rise could reach to nearly 4 times of Ni concentrations at 8a sites of the pristine spinel (4.0% Ni occupancy in pristine powder versus 16% in 0.5 mol fluorine-doped spinel) (Fig. 5a–b).

It is important to note that within the studied range of fluorine substitution, minor traces of LiF (PDF#: 04-0857) was observed which became more pronounced when higher concentrations of fluorine was used. This could possibly imply that there could be a limited solid solubility of the fluorine in the spinel structure (in the

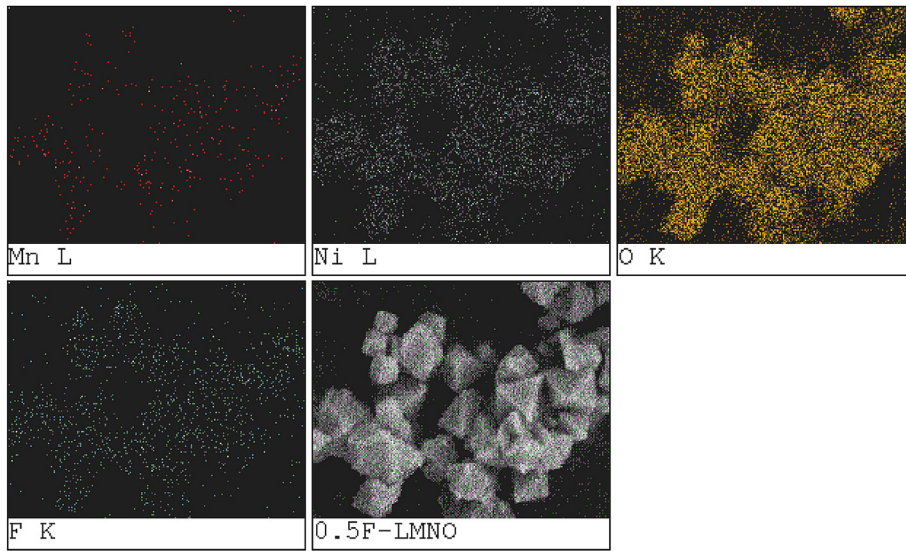


Fig. 6. EDS maps of K_{α} lines for O, and F and L_{α} lines for Mn and Ni in $\text{LiMn}_{1.5}\text{Ni}_{0.5}\text{O}_{3.5}\text{F}_{0.5}$ spinel with accelerating voltage of 5 kV.

range of $x \leq 0.1$) under the studied conditions, as previously identified for 4 V spinels.

In order to clarify fluorine distribution throughout the spinel structure, energy dispersive spectroscopy (EDS) was carried out for spinel with the highest studied fluorine ($x = 0.5$) namely $\text{LiMn}_{1.5}\text{Ni}_{0.5}\text{O}_{3.5}\text{F}_{0.5}$. Fig. 6 illustrates the EDS maps of K_{α} lines for O and F and La lines for Mn and Ni in 0.5 mol fluorine-doped spinel with accelerating voltage of 5 keV. In order to perform the EDS map, the energy windows for Mn, Ni, F, and O were selected based on their excitation energies for K or L lines and corresponding applied accelerating voltage. The selection of accelerating voltage of 5 keV was based on the fact that this energy was sufficient enough to excite the fluorine (677 eV) and oxygen (525 eV) K_{α} lines without having the interference with strong Mn K_{α} (5898 eV) and Ni K_{α} (7477 eV) lines when excitation energy is beyond 7.5 kV.

As shown in Fig. 6, the uniform distribution of the Ni, Mn, O, and F was observed throughout the spinel particles. While the spot intensity in the EDX map can qualitatively reflect the extent of distribution, however cannot be used for quantitative comparison between the elements. The similarity between oxygen and fluorine EDS maps indicates that fluorine atoms were uniformly distributed throughout the grain where the fluorine atoms were expected to be substituted in oxygen sites. The EDS map of fluorine also demonstrated almost no separate phase segregation in the spinel. EDS at higher accelerating voltage of 10 keV (not shown here) was also examined which demonstrated similar F⁻ distribution to 5 keV mapping with lower received fluorine signals to the EDS detector since there was more x-ray interferences from K_{α} lines of Mn (5898 eV) or Ni (7477 eV).

Besides the observation of the uniform EDS map for fluorine it would be beneficial to know the spatial resolution based on accelerating voltage in order to predict approximate depth of fluorine substitution into the spinel particles. The relatively good practical approximation of spatial resolution which is calculated from accelerating voltage and excitation energy can be expressed as [35]:

$$R = 0.064(E_a^{1.68} - E_c^{1.68})/\rho$$

where R is the spatial resolution in μm , E_a accelerating voltage in keV, E_c critical excitation energy in keV and ρ is the mean sample density in g cc^{-1} . By considering the Mn as a major phase and

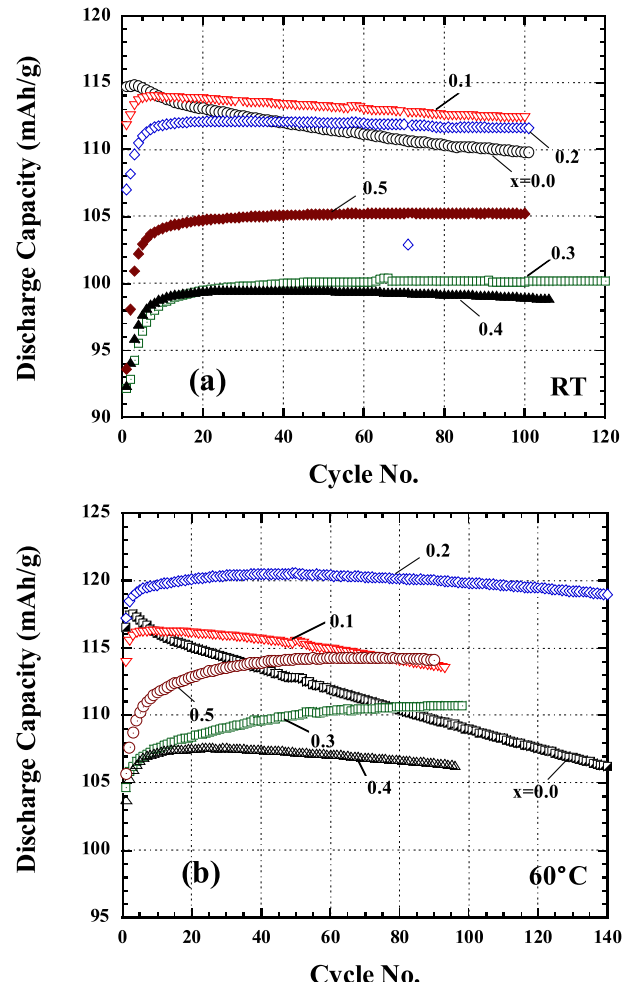


Fig. 7. (a) RT and (b) 60 °C cycling of the fluorine doped $\text{LiMn}_{1.5}\text{Ni}_{0.5}\text{O}_{4-x}\text{F}_x$ ($x = 0, 0.1, 0.2, 0.3, 0.4$, and 0.5 spinels). Cut-off voltage: 5.0–3.5 V; rate: 44 mA g^{-1} .

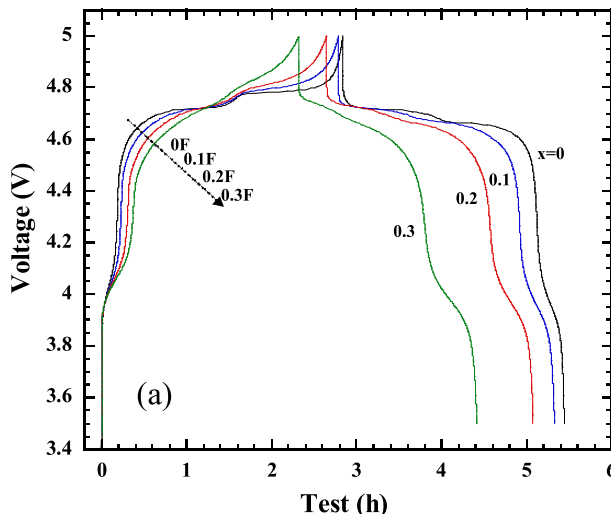


Fig. 8. Voltage profile of the first cycle in (a) fluorine doped $\text{LiMn}_{1.5}\text{Ni}_{0.5}\text{O}_{4-x}\text{F}_x$ ($x = 0, 0.1, 0.2, 0.3$) spinels at room temperature. Cut-off voltage: 5.0–3.5 V; rate: 44 mA g^{-1} .

applying the excitation energies of $\text{Mn } K_{\alpha}$ and L_{α} , the spatial resolution for accelerating voltages of 5 and 10 kV were 0.21 and $0.4 \mu\text{m}$, respectively. This indicated that x-ray signals for fluorine could be received from the core part of particle far ($\sim 400 \text{ nm}$) from the surface.

The uniform fluorine distribution observed in EDS map along with spatial resolution approximation of fluorine from the few hundred nanometers distance within the spinel particles still is not sufficient to explain the presence of LiF (X-ray results) in the doped spinels at $x \geq 0.1$ F. Although the data suggests a solid solution formation, the LiF could be well distributed on a length scale less than a few hundred nanometers.

3.3. Electrochemical properties of F-doped spinels

The electrochemical cycling performance of the fluorine doped LMNO were studied at the rate of 44 mA g^{-1} ($\sim \text{C}/3$) at 24°C (RT) and 60°C . As illustrated in Fig. 7, fluorine substitution for oxygen reduced the initial discharge capacity both at RT and 60°C . In the case of 0.3 mol fluorine, this reduction in capacity was about 10 and 2.3% for RT and 60°C , respectively. As shown in Fig. 7 addition of the

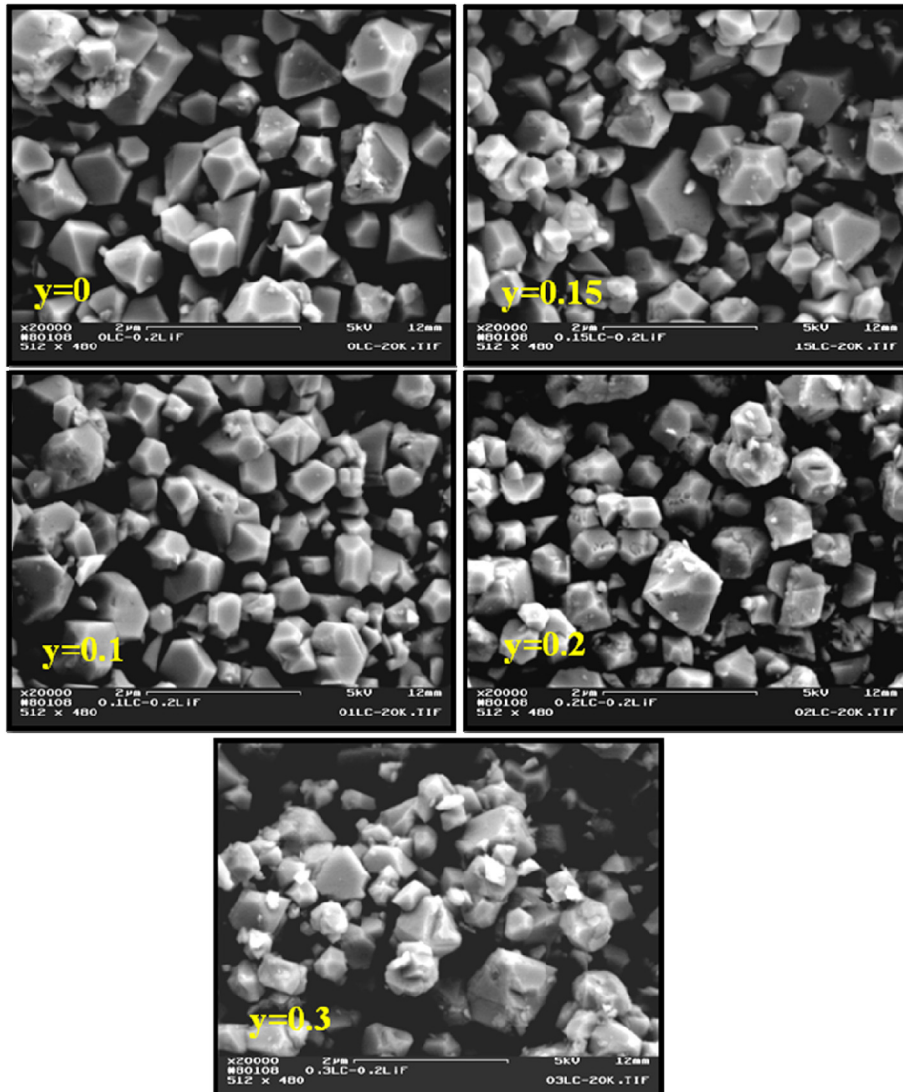


Fig. 9. Field emission scanning electron microscopy (FeSEM) graphs showing the effect of excess Li^+ on particle size and morphology of the $\text{Li}_{1+y}\text{Mn}_{1.5}\text{Ni}_{0.5}\text{O}_{3.8}\text{F}_{0.2}$ ($y = 0, 0.1, 0.15, 0.2, 0.3$) spinels annealed at 800°C -12 h.

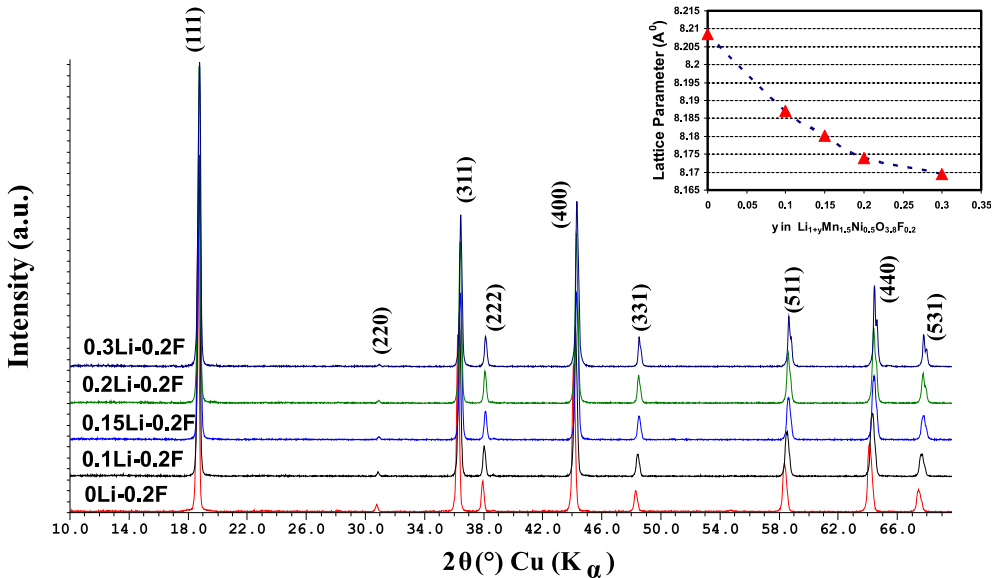


Fig. 10. X-ray diffraction of excess Li^+ ($y = 0, 0.1, 0.15, 0.2, 0.3$) for $\text{Li}_{1+y}\text{Mn}_{1.5}\text{Ni}_{0.5}\text{O}_{3.8}\text{F}_{0.2}$ spinels annealed at 800°C -12 h.

fluorine within the range of $0.1 \leq x \leq 0.3$ improved cycling stability as well as capacity retention over undoped spinel. Fluorine-doped spinels did not show any capacity loss (relative to initial capacity) within the first 100 cycles at room temperature, while the standard spinel, fabricated under similar conditions, experienced 4.3% loss in capacity after 100 cycles (Table 2). In terms of elevated temperature performance (60°C cycling), the capacity loss in un-doped spinel expectedly rose to 6.5% at 100th cycle while in the fluorine doped spinels with dopant amount of $x \geq 0.2$ the discharge capacity was still well above the initial value at 100th cycle.

In order to better understand the improvement in capacity retention, it is beneficial to consider the voltage profile changes upon introduction of fluorine. As shown in Fig. 8, the increase in fluorine systematically increased the capacity of the 4 V plateaus which is a clear indication of an increase in concentrations of Mn^{3+} . It is interesting to witness that the high concentration of Mn^{3+} , led to improved cycling stability at RT and 60°C in fluorine doped spinels, despite the historic issue of the Mn^{3+} in disproportionation to Mn^{2+} and Mn^{4+} and disintegrating the cathode. Another observation on the voltage profile (Fig. 8) was the growth of impedance during the charge cycle. The observed initial impedance could be due to the ionic or electronic impedance formed at the surface of the material which decreases with cycling.

The as-prepared oxy-fluoride spinels resulted in good cycling stability with relatively low capacities which were decreased systematically with F substitution. This could be directly related to the substitution of Ni on the tetrahedral sites as a result of the aforementioned Li non stoichiometry. In order to offset this stoichiometry, and test this theory, the effect of excess Li on fluorine doped spinels was investigated with the goal to repopulate the 8a sites with Li. Among the different F-doped spinels, 0.2 mol fluorine showed an improved cycling stability with the highest columbic efficiency (98%) at 60°C while maintaining the highest capacity retention after 100 cycles at 60°C (Table 2). Due to this superior performance, this composition was selected to examine the effect of different moles of excess Li on the electrochemical properties of the spinel.

3.4. Effect of excess Li in F-doped $\text{Li}_{1+y}\text{Mn}_{1.5}\text{Ni}_{0.5}\text{O}_{3.8}\text{F}_{0.2}$

The effect of excess Li^+ on particle size and morphology of the 0.2 mol fluorine-doped LMNO is illustrated in Fig. 9. The addition

of excess Li^+ decreased slightly the average particle size of spinel material, in contrast to the observation of F-additions. This was confirmed by surface area measurements which revealed an increase in surface area of the Li^+ -added powders (Table 1). Addition of 0.3 mol of excess Li^+ increased the surface area of fluorine-doped spinel (0.2 F-LMNO) by about 21%. Li^+ not only affected the particle size, but also on the morphology of the un-doped spinel. It was shown through the SEM micrograph comparison of 0 and 0.3 mol Li^+ (Fig. 9) that the addition of excess Li has changed the sharp well-faceted particles to a smaller and more circular morphology. The observed two mixed morphologies of round and faceted particles could indicate the presence of second phase; however the high resolution X-ray diffraction did not reveal any detectable second phase. This could possibly indicate that the excess Li^+ minimized the formation of LiF as second phase which had formed in the spinel with 0.2 mol of fluorine. Fig. 10 shows the X-ray diffraction of Li-doped $\text{Li}_{1+y}\text{Mn}_{1.5}\text{Ni}_{0.5}\text{O}_{3.8}\text{F}_{0.2}$ ($0 \leq y \leq 0.3$) spinels. As shown, introduction of excess Li^+ shifted the X-ray diffraction patterns toward higher angles or lower d-spacing and therefore shrank the lattice structure indicating the opposite effect of fluorine substitution on the spinel structure. Addition of excess Li^+ depressed the (220) peak intensity as well as (311)/(111) ratio as shown in Fig. 11 which indicates the replacement of excess Li^+ ions for metal ions in tetrahedral sites, where the metal ions had

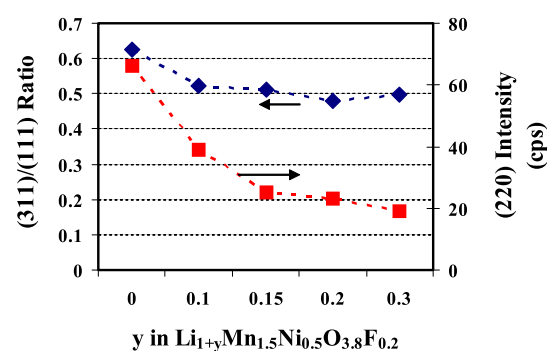


Fig. 11. (311)/(111) intensity ratio and (220) peak intensity for $\text{Li}_{1+y}\text{Mn}_{1.5}\text{Ni}_{0.5}\text{O}_{3.8}\text{F}_{0.2}$ spinels ($y = 0, 0.1, 0.15, 0.2, 0.3$) annealed at 800°C -12 h.

occupied 8a sites upon anion (F^-) substitution. This was confirmed by Rietveld analysis which showed the decrease of transition metal in the 8a scaling with excess Li content (Table 3). The results of refinement for 0.2 mol oxy-fluoride spinels upon introduction of different concentrations of lithium (e.g. 0.1Li, 0.15Li, 0.2Li and 0.3Li) showed a whole pattern fitting (R_{wp}) of 3.92–4.57%. Introduction of 0.1 mol Li to oxy-fluoride spinel (0.2 F) drastically reduced the concentration of Ni atoms in tetrahedral sites of spinel from 12% to 6%. Addition of more lithium to oxy-fluoride spinel further reduced the Ni concentrations in Li sites to about 1%, which was even lower than pristine spinel (metal ion mixing: ~4.01%) (Fig. 12a–b). It appeared that the effect of Li addition on oxy-fluoride spinel was opposite of fluorine effect leading to compensation of the tetrahedral occupation by Ni ions, reduction

in concentrations of Mn^{3+} (lattice parameter) and increase in cell density.

3.5. Electrochemical properties of co-doped (Li^+ and F^-) spinels

The electrochemical performance of the Li doped oxy-fluoride spinels is shown in Fig. 13. Addition of 0.15 mol excess Li noticeably improved the initial discharge capacity of 0.2 mol fluorine-doped spinel from 107.0 mAh/g to 130.8 mAh/g at RT. Further addition of Li decreased the discharge capacity while adversely affecting the RT cycling stability relative to 0.2 mol fluorine-doped spinel without excess Li. For example, the capacity loss for 0 (pristine spinel) and 0.3 mol excess Li spinel (with 0.2 mol fluorine) after 100 cycles at RT was 4.3% and 6.9%, respectively (Table 2).

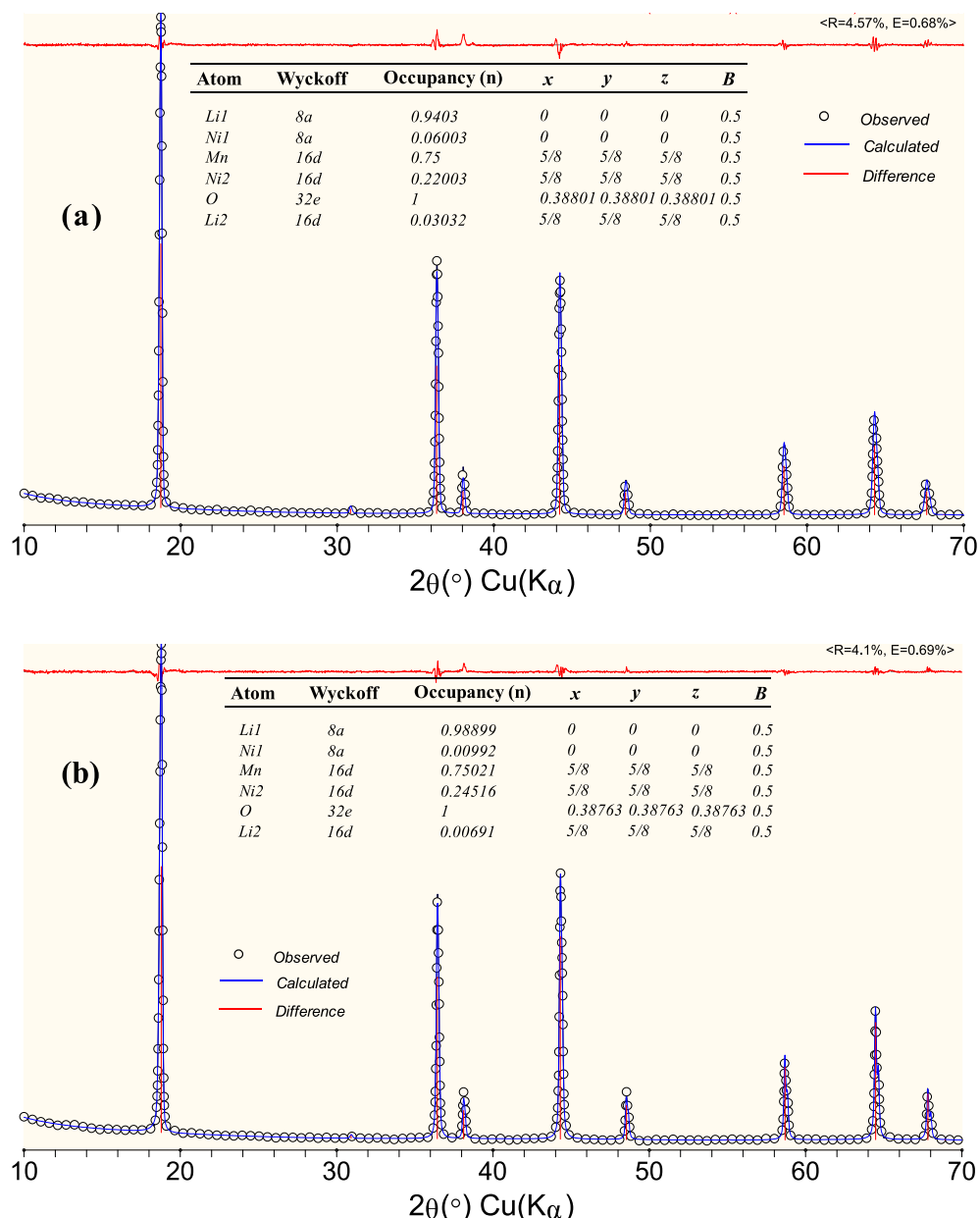


Fig. 12. Structural refinement of (a) 0.1 mol Li doped oxy-fluoride spinel ($Li_{1.1}Mn_{1.5}Ni_{0.5}O_{3.8}F_{0.2}$) (R_{wp} : 4.57%, E: 0.68%; S.G.: $Fd\text{-}3m$, no. 227 or $cF56.1$; origin at $-43m$; $a = 8.18501 \text{ \AA} \pm 0.000184$; Cell vol. = 548.4 \AA^3 ; $\rho = 4.4257 \text{ g cm}^{-3}$) and (b) 0.3 mol Li doped oxy-fluoride spinel ($Li_{1.3}Mn_{1.5}Ni_{0.5}O_{3.8}F_{0.2}$) by Rietveld analysis (R_{wp} : 4.1%, E: 0.69%; S.G.: $Fd\text{-}3m$, no. 227 or $cF56.1$; origin at $-43m$; $a = 8.16576 \text{ \AA} \pm 0.000096$; Cell vol. = 544.5 \AA^3 ; $\rho = 4.4584 \text{ g cm}^{-3}$).

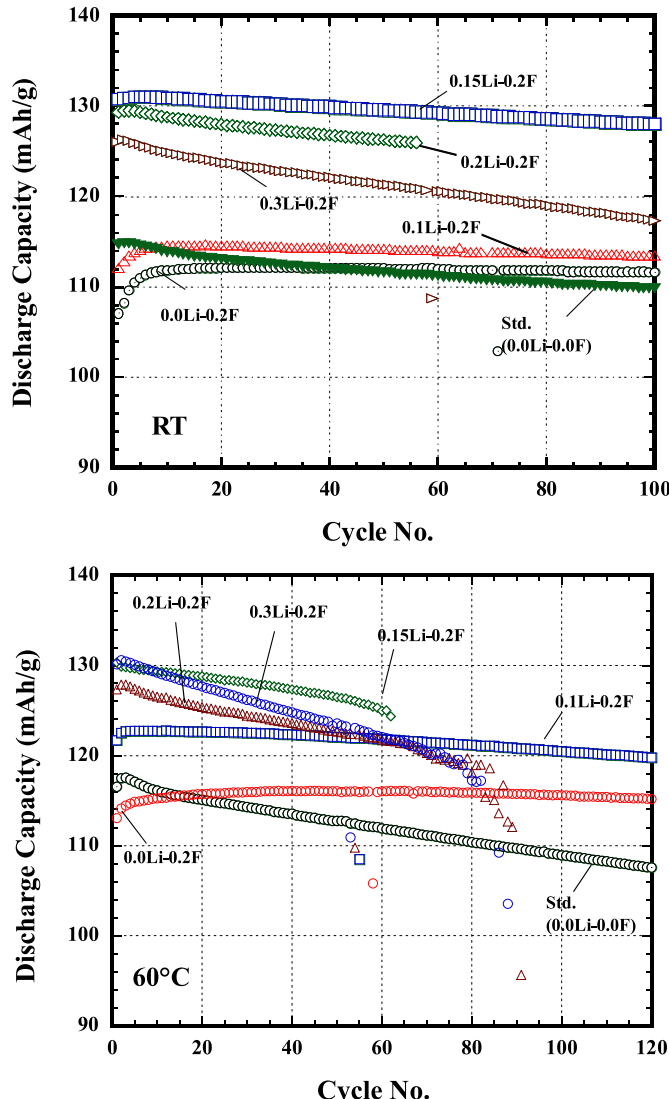


Fig. 13. RT and 60 °C cycling of the Li doped $\text{Li}_{1+y}\text{Mn}_{1.5}\text{Ni}_{0.5}\text{O}_{3.8}\text{F}_{0.2}$ ($y = 0, 0.1, 0.15, 0.2, 0.3$) Spins. Cut-off voltage: 5.0–3.5 V; rate: 44 mA g^{-1} .

The similar trend of change in capacity and cycling stability was observed in Li-doped cells cycled at 60 °C. An increase in capacity loss was directly related to the excess Li content. The higher excess Li, the higher capacity loss. For example, for 0.3 mol excess Li the capacity loss was almost doubled relative to 0 mol excess Li after 50 cycles at 60 °C. As shown in Fig. 13, the catastrophic failure was observed in Li concentrations of $y > 0.1$ which caused the higher impedance rise early before reaching to their 100 cycles. In the case of the Li concentrations of $y \leq 0.1$, no sudden failure was observed over the one hundred cycles at 44 mA g^{-1} .

As shown from the electrochemical results, Li addition had an opposite effect of fluorine substitution. This was also observed through the voltage profile change upon increasing the Li concentrations. Fig. 14 demonstrates the effect of the Li addition on voltage profile of the 0.2 mol F-doped spinel. Increase in excess Li diminished the 4 V plateau due to an increase in average Mn oxidation state. Addition of excess Li also lowered the first cycle impedance with a more pronounced $\text{Ni}^{2+}/\text{Ni}^{4+}$ redox plateaus.

Fig. 15 demonstrates the capacity and rate capability of the F⁻ and Li-doped spinels. As shown earlier, fluorine substitution increased the particle size and decreased the surface area through

its fluxing effect. In contrast, the Li addition demonstrated the opposite effect of fluorine and led to decrease in average particle size and increase in surface area. The effect of both dopants on particle size directly influenced their rate capabilities through the increase/decrease in Li diffusion path. In addition to particle size effect, the rate could also be affected by electronic/ionic barriers which limit the ionic or charge transfer especially at higher current densities.

To evaluate the long term cycling stability of the pristine and doped spinels at elevated temperature (e.g. $T = 60$ °C), galvanostatic cycling of 0.2 F-doped spinel was evaluated with two nano- and micron-sized pristine spinels. Fig. 16 shows the discharge capacity retention of nano size (~ 50 nm, $5.5 \text{ m}^2 \text{ g}^{-1}$) and micron size ($0.8\text{--}1 \mu\text{m}$, $1.6 \text{ m}^2 \text{ g}^{-1}$) spinels along with 0.2 mol-doped oxy-fluoride spinel ($1.82 \text{ m}^2 \text{ g}^{-1}$) cycled at 60 °C under the current density of 44 mA g^{-1} (~C/3). As shown, a cell containing the nano sized pristine spinel displayed a higher fading rate relative to micron sized spinel despite its high initial discharge capacity. This effect primarily was due to the higher extent of electrolyte degradation on high surface area electrode. This relatively known phenomenon for nano-sized spinel led to rapid increase in impedance followed by cell's early failure. Micron-sized spinel did not show any abrupt decrease in impedance and capacity retention was 81.3% after 320 cycles. The capacity retention was the highest in 0.2 mol oxy-fluoride spinel whereas no capacity loss was observed within the first 200 cycles with capacity retention of 96.1% after 320 cycles. While we continued cycling of the oxy-fluoride cell over 1400 cycles, there was no sharp increase in cell's impedance over the long cycling period and 50.7% of discharge capacity was maintained after 1418 cycles. Relatively low impedance observed in oxy-fluoride spinel could be due to the formation of fluoride-based compound(s) at the surface of the spinel particles, upon introduction of fluorine. This may suggest intrinsic and extrinsic contributions of the fluorine dopant on improving the electrochemical performance of the spinel. While the origin of superior cycling performance of oxy-fluoride spinel requires further investigation, fluorine substitution clearly showed a long term cycling stability and high capacity retention at 60 °C. Based on the results presented here, 8a occupancy of Ni in the 8a sites and the development of well-developed morphology may have also contributed to an improved performance of the spinel.

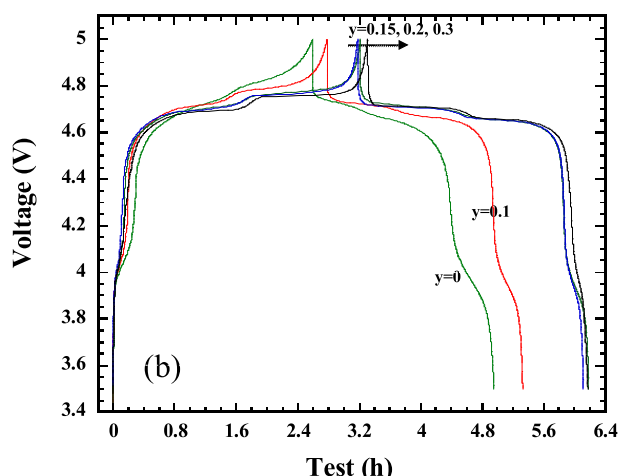


Fig. 14. Voltage profile of first charge and discharge for Li doped $\text{Li}_{1+y}\text{Mn}_{1.5}\text{Ni}_{0.5}\text{O}_{3.8}\text{F}_{0.2}$ ($y = 0, 0.1, 0.15, 0.2, 0.3$) spinels at room temperature. Cut-off voltage: 5.0–3.5 V; rate: 44 mA g^{-1} .

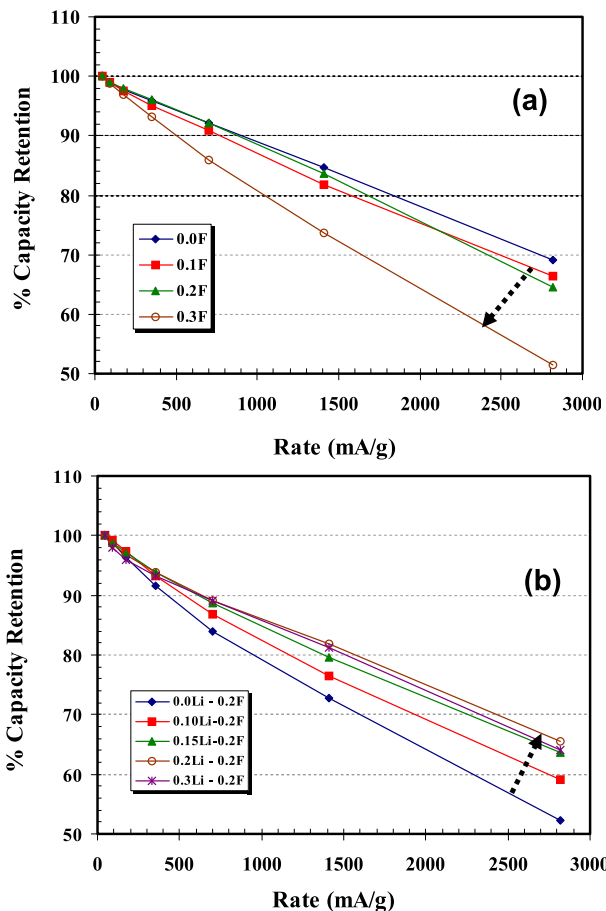


Fig. 15. Effect of (a) fluorine and (b) excess Li on capacity and rate capability of $\text{Li}_{1+y}\text{Mn}_{1.5}\text{Ni}_{0.5}\text{O}_{4-x}\text{F}_x$ ($0 \leq x, y \leq 0.3$) spinels at room temperature (24 °C). Cut-off voltage: 5.0–3.5 V; rate: 44–2864 mA g⁻¹.

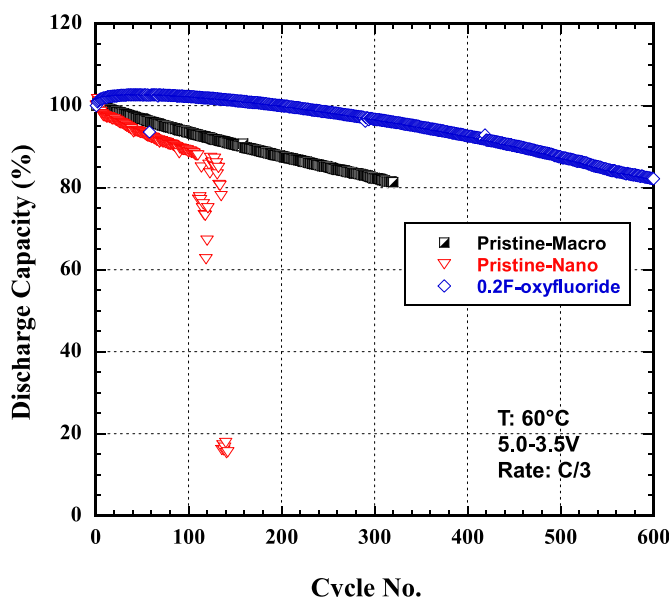


Fig. 16. 60 °C discharge capacity retention of nano- and micron-sized spinels compared with 0.2 mol oxy-fluoride spinel. Cut-off voltage: 5.0–3.5 V; rate: 44 mA g⁻¹.

4. Summary and conclusion

The effect of fluorine and Li addition on physical, microstructure and electrochemical properties of $\text{Li}_{1+y}\text{Mn}_{1.5}\text{Ni}_{0.5}\text{O}_{4-x}\text{F}_x$ ($0 \leq x \leq 0.5, 0 \leq y \leq 0.3$) spinels synthesized through the newly developed solid state process was studied. Fluorine substitution in oxygen sites reduced the Mn oxidation state and led to a growth of (220) peak as an indication of metal ions presence in 8a site. The opposite effect was observed in Li introduction where the Mn valence state increased and more Li occupied the tetrahedral sites of the spinel. This was also confirmed by structural refinement which showed an increasing numbers of Ni and Li atoms at 8a and 16d sites, respectively, upon increasing the fluorine concentrations. The trend was reversed when excess Li was introduced into spinel structure. Fluorine doped spinels showed improved cycling stability with excellent capacity retention at 60 °C while the Li-doped oxy-fluorides were demonstrated higher capacity loss and lower columbic efficiency.

Acknowledgments

Research was sponsored by the Army Research Laboratory and was accomplished under cooperative agreement number W911NF-06-2-0044. The views and conclusions contained in this document are those of the authors and should not be interpreted as representing the official policies, either expressed or implied, of the Army Research laboratory or the U.S. Government. The U.S. Government is authorized to reproduced and distribute reprints for Government purposes notwithstanding any copyright notation heron.

References

- [1] K. Amine, H. Tukamoto, H. Yasuda, Y. Fujita, J. Electrochem. Soc. 143 (5) (1996) 1607–1613.
- [2] Y. Gao, K. Myrtle, M. Zhang, J.N. Reimers, J.R. Dahn, Phys. Rev. B 54 (23) (1996) 670–675.
- [3] Q. Zhong, A. Bonakdarpour, M. Zhang, Y. Gao, J. Dahn, J. Electrochem. Soc. 144 (1997) 205.
- [4] T. Ohzuku, S. Takeda, M. Iwanaga, J. Power Sources 81–82 (1999) 90–94.
- [5] J.-H. Kim, S.-T. Myung, C.S. Yoon, S.G. Kang, Y.-K. Sun, Chem. Mater. 16 (2004) 906.
- [6] H.C. Wang, C.H. Lu, J. Power Sources 119 (2003) 738.
- [7] T. Ohzuku, K. Ariyoshi, S. Takeda, Y. Sakai, Electrochim. Acta 46 (2001) 2327.
- [8] M.E. Arroyo y de Domípablo, J. Morales, J. Electrochim. Soc. 153 (2006) A2098–A2102.
- [9] S.H. Wu, H.J. Su, Mater. Chem. Phys. 78 (2002) 189–195.
- [10] H. Kawai, M. Nagata, H. Kageyama, H. Tukamoto, A.R. West, Electrochim. Acta 45 (1999) 315.
- [11] S.-H. Park, S.-W. Oh, S.-T. Myung, Y.-K. Sun, Electrochim. Solid-State Lett. 7 (11) (2004) A451–A454.
- [12] U. Lafont, C. Locati, E.M. Kelder, Solid State Ionics 177 (2006) 3023–3029.
- [13] R. Alcantara, M. Jaraba, P. Lavela, J.M. Lloris, C. Perez Vicente, J.L. Tirado, J. Electrochim. Soc. 152 (1) (2005) A13–A18.
- [14] B. Markovsky, Y. Talyossef, G. Salitra, D. Aurbach, H.-J. Kim, S. Choi, Electrochim. Commun. 6 (2004) 821.
- [15] D. Aurbach, B. Markovsky, Y. Talyossef, G. Salitra, H.-J. Kim, S. Choi, J. Power Sources 162 (2006) 780.
- [16] Y.-K. Sun, Y.-S. Lee, M. Yoshio, K. Amine, Electrochim. Solid-State Lett. 5 (5) (2002) A99–A102.
- [17] Y. Fan, J. Wang, Z. Tang, W. He, J. Zhang, Electrochim. Acta 52 (2007) 3870–3875.
- [18] A.M. Kannan, A. Manthiram, Electrochim. Solid-State Lett. 5 (7) (2002) A167–A169.
- [19] J. Arrebola, A. Caballero, L. Hernan, J. Morales, E. Rodriguez Castellon, J.R. Ramos Barrado, J. Electrochim. Soc. 154 (3) (2007) A178–A184.
- [20] S.-H. Kang, M.M. Thackeray, J. Electrochim. Soc. 155 (4) (2008) A269–A275.
- [21] N.M. Hagh, F. Cosandey, S. Rangan, R. Bartynski, G.G. Amatucci, J. Electrochim. Soc. 157 (3) (2010) A305–A319.
- [22] G.G. Amatucci, A. Blyr, C. Schmutz, J.M. Tarascon, Prog. Battery Battery Mater. 16 (1) (1997).
- [23] G.G. Amatucci, N. Pereira, T. Zheng, I. Plitz, J.M. Tarascon, J. Power Sources 81 (1999) 39.
- [24] G.G. Amatucci, N. Pereira, T. Zheng, J.M. Tarascon, J. Electrochim. Soc. 148 (2001) A171.

- [25] G.G. Amatucci, N. Pereira, J. Fluor. Chem. 128 (2007) 243–262.
- [26] Y.-J. Kang, J.-H. Kim, Y.-K. Sun, J. Power Sources 146 (2005) 237–240.
- [27] J.T. Son, H.G. Kim, J. Power Sources 147 (2005) 220–226.
- [28] W. Choi, A. Manthiram, Electrochim. Solid-State Lett. 9 (5) (2006) A245–A248.
- [29] K. Kubo, S. Arai, S. Yamada, M. Kanda, J. Power Sources 81–82 (1999) 599–603.
- [30] A.R. Naghash, J.Y. Lee, Electrochim. Acta 46 (2001) 2293–2304.
- [31] S.-H. Kang, I. Belharouak, Y.-K. Sun, K. Amine, J. Power Sources 146 (2005) 650–653.
- [32] N.M. Hagh, G.G. Amatucci, J. Power Sources 195 (2010) 5005–5012.
- [33] M. Kunduraci, G.G. Amatucci, J. Electrochem. Soc. 153 (2006) A1345.
- [34] J.M. Tarascon, W.R. McKinnon, F. Coowar, T.N. Bowmer, G.G. Amatucci, D. Guyomard, J. Electrochem. Soc. 141 (6) (1994) 1421–1431.
- [35] J. Friel, X-ray and Image Analysis in Electron Microscopy, Princeton Gamma-Tech, Princeton, NJ, 1995.